energies

MDPI

Article

Experimental and Simulation Investigation of Performance of Scaled Model for a Rotor of a Savonius Wind Turbine

Kumail Abdulkareem Hadi Al-Gburi [1], Balasem Abdulameer Jabbar Al-quraishi [2], Firas Basim Ismail Alnaimi [3,*], Ee Sann Tan [1] and Ali Hussein Shamman Al-Safi [4]

[1] Department of Mechanical Engineering, Universiti Tenaga Nasional (UNITEN), Kajang 43000, Malaysia
[2] Engineering Technical College of Najaf, Al-Furat Al-Awsat Technical University, Najaf 31001, Iraq
[3] Power Generation Unit, Institute of Power Engineering (IPE), Universiti Tenaga Nasional (UNITEN), Kajang 43000, Malaysia
[4] Computer Techniques Engineering Department, Al-Mustaqbal University College, Hillah 51001, Iraq
* Correspondence: firas@uniten.edu.my

Abstract: Renewable energy sources are preferred for many power generation applications. Energy from the wind is one of the fastest-expanding kinds of sustainable energy, and it is essential in preventing potential energy issues in the foreseeable future. One pertinent issue is the many geometrical alterations that the scientific community has suggested to enhance rotor performance features. Hence, to address the challenge of developing a model that resolves these problems, the purpose of this investigation was to determine how well a scaled-down version of a Savonius turbine performed in terms of power output using a wind tunnel. Subsequently, the effect of the blockage ratio produced in the wind tunnel during the chamber test on the scaled model was evaluated. This study discusses the influences of various modified configurations on the turbine blades' torque and power coefficients (*Cp*) at various tip speed ratios (*TSRs*) using three-dimensional (3D) unsteady computational fluid dynamics. The findings showed that the scaled model successfully achieved tunnel blockage corrections, and the experimental results obtained can be used in order to estimate how the same turbine would perform in real conditions. Furthermore, numerically, the new models achieved improvements in *Cp* of 19.5%, 16.8%, and 12.2%, respectively, for the flow-guiding channel (FGC at $\Phi = 30°$), wavy area at tip and end (WTE), and wavy area on the convex blade (WCB) models in comparison to the benchmark S-ORM model and under identical wind speed conditions. This investigation can provide guidance for improvements of the aerodynamic characteristics of Savonius wind turbines.

Keywords: wind energy; Savonius wind turbine; S-ORM model; coefficient of power; CFX analysis; rotor experimental testing

check for updates

Citation: Al-Gburi, K.A.H.; Al-quraishi, B.A.J.; Ismail Alnaimi, F.B.; Tan, E.S.; Al-Safi, A.H.S. Experimental and Simulation Investigation of Performance of Scaled Model for a Rotor of a Savonius Wind Turbine. *Energies* **2022**, *15*, 8808. https://doi.org/10.3390/en15238808

Academic Editors: Galih Bangga and Martin Otto Laver Hansen

Received: 12 October 2022
Accepted: 18 November 2022
Published: 22 November 2022

1. Introduction

Electricity production from renewable sources has increased in recent years, making it one of the most significant commodities in contemporary civilization and one that has no negative impact on the environment [1]. Wind power is widely regarded as one of the most exciting and potentially useful new kinds of energy because of its seemingly limitless potential. Wind turbines have also been used for mechanical needs and energy production because of their widespread availability, low cost, and ease of assembly. Wind turbine rotors typically fall into two categories: horizontal axis wind rotors (HAWRs) and vertical axis wind rotors (VAWRs). These are named based on the orientation of their revolving shafts. HAWRs, well-known for their better power efficiency, have long been relied upon when efficient power is needed. There are several advantages to employing a VAWR (particularly a Savonius model): a higher starting torque, a lower cut-in speed, self-starting operation, and a low noise level [2].

In view of this, the Savonius wind turbine, with its vertical axis, has become a popular choice to produce electricity from wind power in small-scale applications [3]. Improvements upstream of the turbine can be achieved by utilizing the wake energy for different boundary conditions [4]. Consequently, applying the V-linear layout-arrangement turbine array when considering the wake energy in a large wind farm was found to result in 11%, 5%, 22.89%, and 21% respective increases in total power [5–8]. Moreover, combinations of other Savonius rotors, which rotate in opposite directions, have been found to increase performance by 38%, 80%, and 6.8% [9–11] compared to conventional Savonius rotors. The accumulative inner arc results have been determined to be 17.81%, 11.34%, 32.9%, 41%, and 10%, respectively. This shows an improvement over the conventional configuration [12–16], but a two-dimensional (2D) simulation was used to avoid complex geometries. One of the main methods used to improve rotor performance is adding an auxiliary structure, such as a casing, nozzle, deflector, cylindrical cowling, rotor house, omni-directional guide vane, or circular cylinder [17–27]. However, these structures might impact other efficiency criteria, such as the overlap ratio and end plates, and require reevaluation following installation.

Three rotor parameters—factor in shape, overlap ratio, and tip speed ratio (*TSR*)—are used as independent variables to create a regression formula and determine the best parameter set for the power coefficients (*Cp*). This is undertaken using Minitab software during the experiment design [28]. Note that the opening the valve on the blades at the best angle has become a good technique and approach, exhibiting a 14% improvement in performance [29]. Furthermore, fluid–structure interaction (FSI) modeling has been used in the analysis of the boundaries of a wind turbine's blades and can define the strain (displacement) using an elastic stiffness matrix [30]. However, flexible designs rely on wind speed and the *TSR*, whereas Savonius turbines, which have rigid blades, are not subject to this limitation. Moreover, genetic algorithms (GAs) can be used to discover innovative geometries automatically by using methods that produce random geometries, increasing the *Cp* and achieving a maximum substantial improvement of up to 33% [31–36]. Nevertheless, to prove this assumption is correct, this research utilized a technique called digital image processing (DIP) with the assistance of an optimization technique that generated random models. The particle swarm optimization (PSO) algorithm was applied to determine the optimal design parameters in accordance with the response of a surface model developed using the Kriging [37] and Taguchi [38] methods. The difference in *Cp* change between a single-stage rotor and multiple-stage rotor indicated that the extra segmentation of rotor plates reduced the rotor's effectiveness. It is simple to envisage that the characteristics of a multi-stage rotor directly result from its more challenging production process [39,40]. One investigation has been carried out with the Savonius turbine utilizing a configuration of slotted blades on the rotor, which made it possible to draw a conclusion based on the findings and the study that the installation of slotted blades on Savonius wind turbines can increase their overall performance [41]. Here, the *Cp* increased with the *TSR,* with a maximum value of 2.5% [42].

Many researchers have investigated the crucial optimized geometric parameters that would significantly improve performance. The investigation carried out by M. Niyat Zadeh et al., used COMSOL software to simulate a Savonius-type turbine helical configuration at two different wind speeds (6 and 8 m/s). This was performed by considering the influence of one important parameter on performance: Bach's section effect [43]. Mariem Lajnef et al., and A. Damak et al., conducted experimental research using a three-dimensional (3D) printer to model a Savonius rotor of a helical type in a wind tunnel, where the rotor's static and dynamic design factors were studied [44,45]. On the other hand, Nur Alom et al., utilized vent augmenter blades to decrease the rotor's drag-negative force using unsteady 3D simulations of the vented elliptical profile rotor. This was done by estimating its drag force (CD) and lift force (CL) [46] after the tests were conducted in a wind tunnel [47]. Likewise, S. Meri et al., proposed an elliptical inner wavy blade through unsteady two-dimensional (2D) simulations in ANSYS Fluent and experimentally using a wind tunnel. Further results have detected a considerable increase in power relative to the classical model [48]. Elmekawy et al. [49] performed computational analyses to examine the impact of varying the twisting angle on the blade rotor. W. A. El-Askary et al. [50] suggested a twisted Savonius rotor with a modified profile and a twist angle of 45 degrees was investigated in both experimental and computational research. An investigation has been carried out to identify the ideal overlap ratio of twisted blades and size ratio of endplates, as well as their influence on the aerodynamic performance of a twisted Savonius rotor [51]. M. Tahani et al. [52] proposed enhancements that can be summed up as follows: (1) a Savonius rotor twist with an adjustable cutting plane, (2) a plane that has a conical shaft and a twisted Savonius rotor, (3) a Savonius rotor that twists with a conical shaft and a movable cut plane, and (4) a conical shaft and a movable cut plane making up a twisted wind rotor.

Based on the above relevant research analyses, it can be observed that geometric and operating characteristics influence the Savonius wind turbine's performance. Moreover, the installing space, along with wide range of proposed methods and approaches, were shown to affect the efficiency of typical Savonius wind turbines, as summarized in Figure 1. However, one of the critical issues in developing the Savonius wind turbine is that the rotor performance is less efficient than other types of wind turbines, such as the Darrius VAWR and Archimedes wind turbine HAWR.

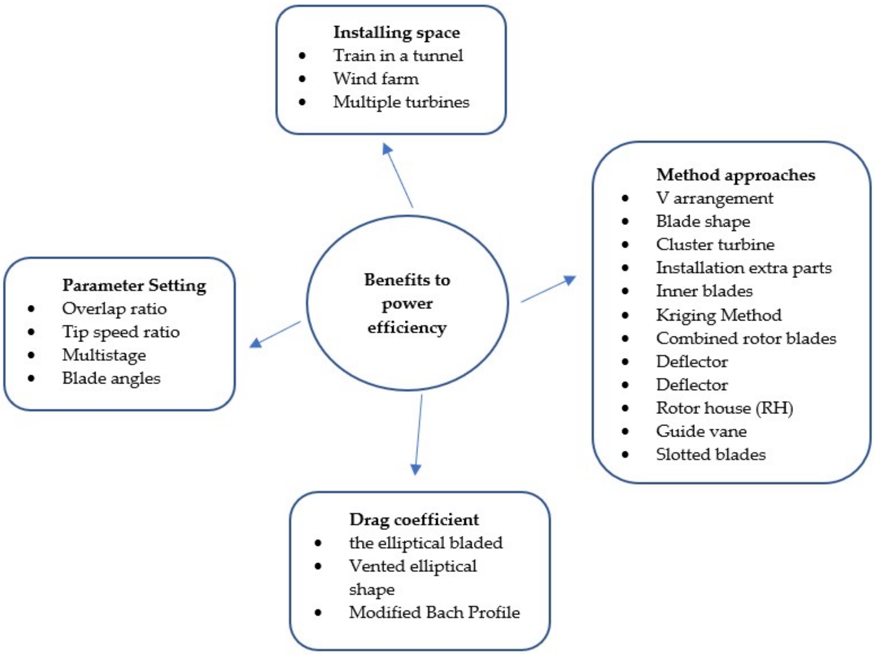

Figure 1. Benefit categories for Savonius wind turbine efficiency.

In this study, we compared a chosen basic model [48] and an identical scaled-down version of the same basic model to study the effect of the blockage ratio through the use of 3D simulation and a wind tunnel experiment. Subsequently, we conducted computational fluid dynamics (CFD) analysis of the proposed new models, which was directed towards developing the effectiveness of Savonius wind turbines in operation and minimizing the quantity of negative torque. However, there are no previously recorded research efforts that address the issues of performance enhancement and profile modification for the two-blade elliptical Savonius turbine with inner wavy area configuration proposed in this investigation. The novelty of this work consists in the adjustment of the wavy area positions along the concave and convex blades and the further addition of a flow guide channel with different angles to the wavy blade profile. This method does not need a complex fabrication process; therefore, it can reduce the device's production costs and be performed in actual conditions.

2. Performance Estimation Calculations

The power produced by the wind turbine rotor was estimated by multiplying the rotor torque (T) by the rotor angular velocity (ω). One other significant factor definition used was the wind's available energy, which was measured by the coefficient of power (Cp) with respect to the tip speed ratio (TSR). Note that the Betz law provides the upper bound for the efficiency with which wind energy may be converted into usable energy. Accordingly, the C_P describes the maximum efficiency with which the kinetic energy of the air flowing from the wind turbine blades can be turned into rotational energy [53]. The C_P and TSR formula is as follows:

$$C_P = \frac{P_{turbine}}{P_{\ wind}} = \frac{T\omega}{0.5\ \rho\ A\ V_\infty^3}, \tag{1}$$

$$TSR = \frac{\omega\ R}{V\infty}. \tag{2}$$

Another definition is the that of the torque coefficient (C_T), which defines the ratio of the rotor's actual torque (T) to the theoretical torque $(T_{\ w})$ generated by the wind [54].

$$C_T = \frac{Actual\ torque}{Theortical\ torque} = \frac{T_{turbine}}{T_{\ w}} = \frac{T}{0.5\ \rho\ A\ R\ V_\infty^2} = \frac{C_P}{TSR}, \tag{3}$$

where ρ is the density of air, which is equal to 1.165 kg/m^3 at 30 °C; T represents torque (N-m); $T_{\ w}$ represents the theoretical torque; A represents the swept blade area (m^2); R represents the effective radius of the turbine (m); and $V\infty$ is the velocity of incoming air (m/s).The experiment's generated torque was computed as follows [45].

$$T_{turbine} = F\ r = 9.81\ (W - S)(rp + dr), \tag{4}$$

in which the pulley load (F) and pulley radius (r) are used. W is the side tight tension (kg), S is the side slack (kg), rp is the pulley radius (m), and dr is the string nylon diameter (m).

3. Methods

This work modified (two adjustments were carried out) the original Savonius rotor's dimensions and geometry using three-dimensional (3D) modeling in Solid Works and simulation in Ansys CFX 2020 R2 in tandem with experimental analysis. However, the size of the test section of the aerodynamic lab was restricted, which led to a different range for the blockage ratio (BR) in this investigation. Note that the definition of the BR is the ratio of the rotor's swept area ($A = H \times D$) to the flow cross-section area ($At = L \times W$). The blockage percentage in this study was under 30%, which is acceptable [55]. Therefore, no blockage correction measures were used or applied [56]. For the comparison of results, the findings were reported against the dataset with the highest power coefficient (Cp) [57]. The first adjustment defined a numerical and experimental model. Here, the small model was tested by scaling down the rotor size of the original model based on the scale factor (SF) procedure [58]. For this, it was necessary to use enough experimental procedures to measure the output performance of the configured turbine and computational fluid dynamics (CFD) simulations. To preserve the same BR, a 1:1.3 scale model of the original rotor model (S-ORM) was configured and erected in the wind tunnel test section. The second adjustment involved the modification of the blade shape for multiple configurations, resulting in new models with optimal parametric geometry and utilizing ANSYS CFX to investigate the aerodynamic qualities of the modified models. A flowchart detailing the relationship between the experiment and simulation of the processes and the connection with the new modified model is shown in Figure 2.

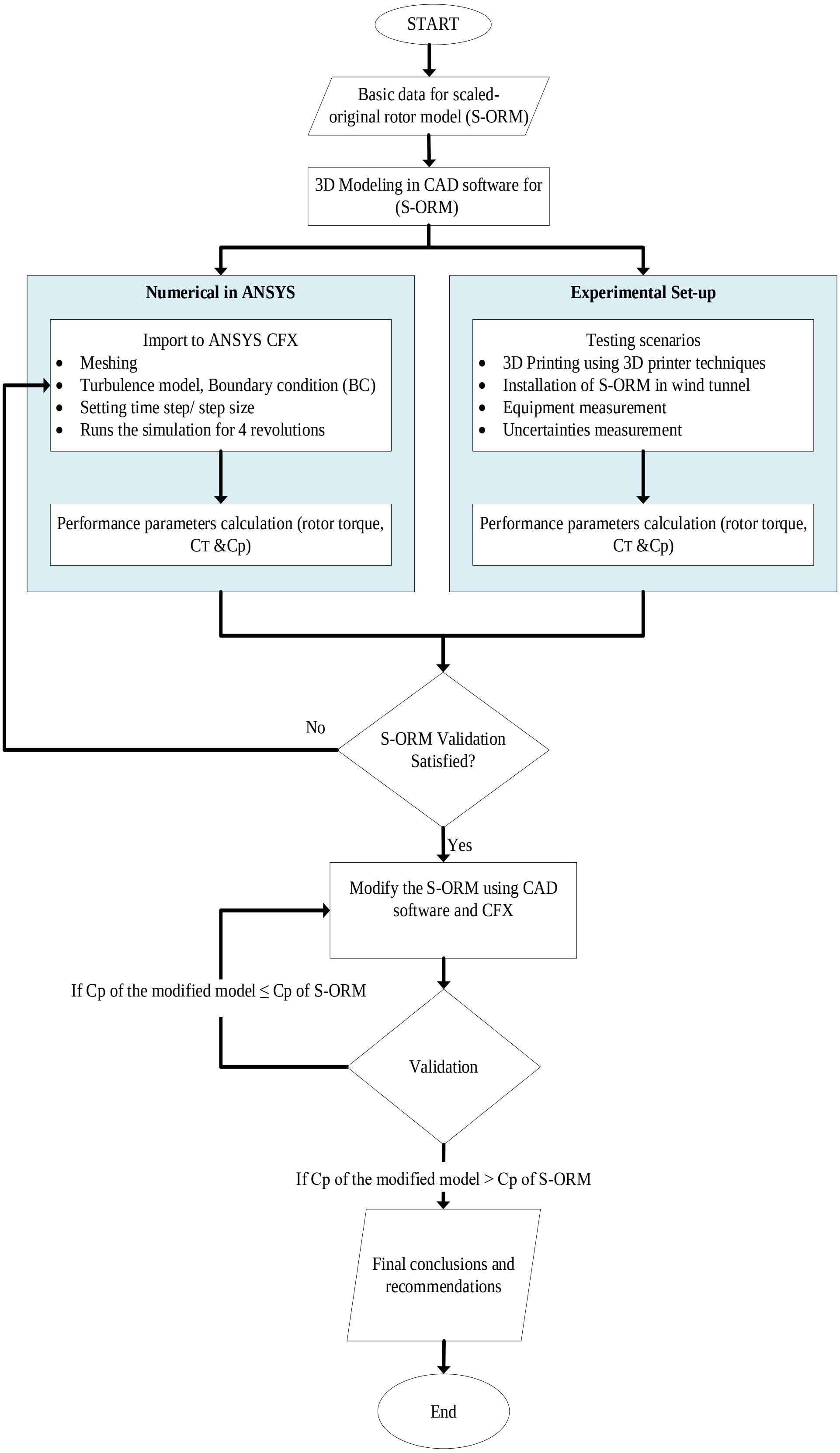

Figure 2. Flow chart detailing the procedure steps for the experiment and simulation in the study.

3.1. Establishment of Geometric Model

This work investigated two elliptical blades' inner wavy areas (WAs) in Savonius turbine models. Figure 3 shows the key features and dimensions of the geometry employed.

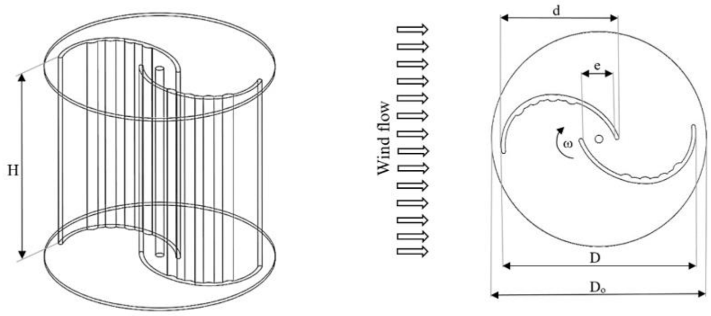

Figure 3. S-ORM geometry employed in the computational and experimental models with H/D = 1, e = D/5 = d/3 ≈ 0.2, and BLN = 2.

In accordance with the definitions of each term, H is the rotor height, D denotes the diameter rotor, d represents the length of the blade chord, e is the distance between overlaps, and Do expresses the end plate's diameter. The investigation focused on two input parameters of the geometrical numerical model that affected the model's behavior. Firstly, the aspect ratio (AR) was defined as the ratio found by subtracting H from D using Equation (5) [59]. Second, the overlap ratio (OR) operator connected elements e and d, similarly to Equation (6) [59]. Furthermore, the performance of the model was dependent on the frontal swept area of turbine rotor A, which was evaluated using Equation (7) [45].

$$AR = \frac{H}{D}, \tag{5}$$

$$OR = \frac{e}{d}, \tag{6}$$

$$A = H \times D. \tag{7}$$

The software packages Solid Works and ANSYS CFX were adopted to design the geometry and computational domain in two stages. The proposed rotor's dimensions were derived from the original model in the first stage. In the second stage, the geometry of the original elliptical model (benchmark model), as highlighted earlier, was modified by considering the modification of the wavy area positions and adding a flow-guiding channel (FGC). Furthermore, a comparison between a benchmark Savonius rotor and ten rotor blades is proposed in this study, as shown in Figure 4. A Savonius rotor was installed vertically on the z-axis, with the flow oriented transversely on the y-axis. Subsequently, the number of blades on the rotor was fixed at two; the maximum rotor diameter of Do was 165 mm, while the maximum H was 150 mm. Therefore, D equaled 150 mm of the rotor. In terms of thickness, the rotor blade was assumed to be 3 mm, with an AR of 1 (H/D), an OR of 0.2, and several stages of 1. Within the scope of this investigation, in order to define an innovative blade geometry in Solid Works software, we considered ten different configuration to enhance the performance of the base profile. First, the rotor models (M1, M2, M3, and M4) defined the change in WA positions, which were named WTE, WCB, FEW, and TQW. Secondly, the rotor models (M5, M6, M7, M8, M9, and M10) involved adding the FGC to the WA in the vertical axis elliptical wind blade profile models, for which the flow-guiding channel (FGC) model with fixed L equaled 0.33d at different angle orientations (Ψ).

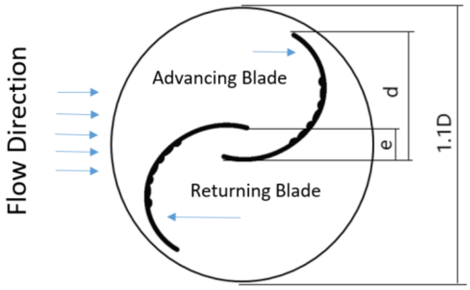

Benchmark S-ORM model

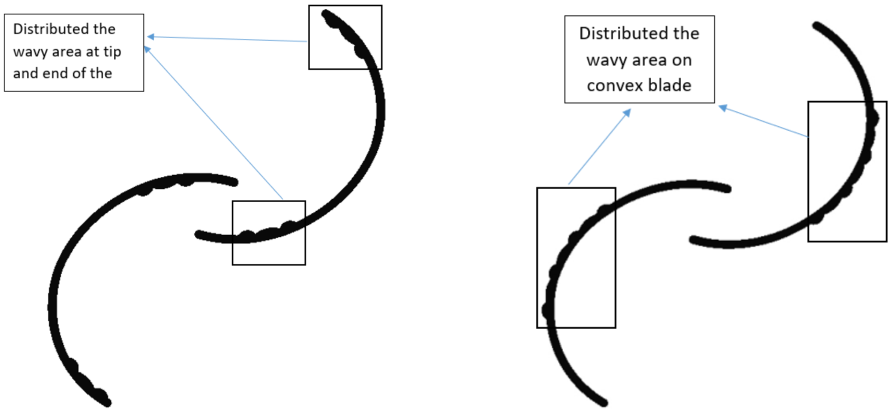

(**a**) WTE model 1 (M1) (**b**) WCB model 2 (M2)

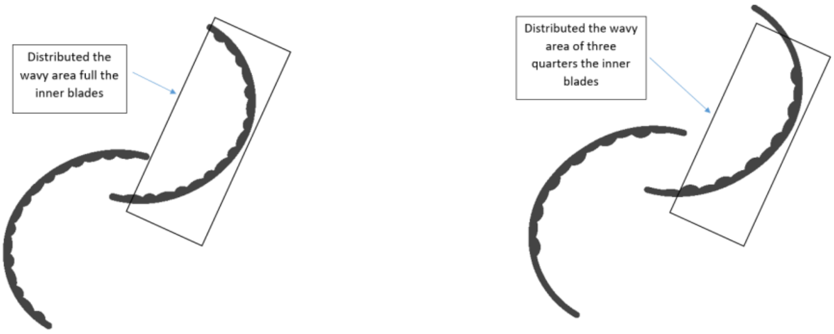

(**c**) FEW model 3 (M3) (**d**) TQW model 4 (M4)

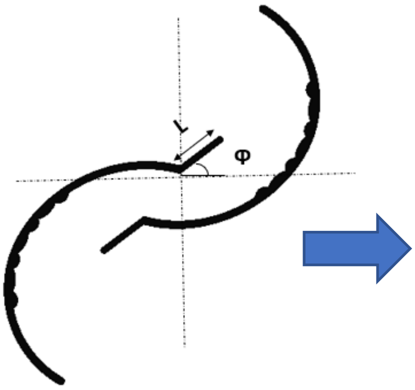

Model no.	L	Φ
M5	0.33d	25°
M6		30°
M7		37°
M8		40°
M9		55°
M10		65°

(**e**) FGC model

Figure 4. Rotor cross-sections of benchmark model and modified profiles.

3.2. Numerical Model

In the examined cases, this work used ANSYS CFX 2020 R2 transient flows for numerical simulation with the scaled model. The methodology that was applied during the building of the CFX CFD model was formulated based on recommendations from relevant studies [12,51,52,60] and on previous work by the authors [48,57]. The Navier–Stokes equations describe the fluid dynamics of a 3D incompressible Newtonian fluid flow. ANSYS CFX was utilized to solve these equations, and the numerical model was rendered accurate to second-order high-resolution time using the finite-volume method (FVM). Based on previous investigations [61], the shear stress transport (SST) model was selected as the turbulence model. When the SST turbulence model was used in a 3D simulation for this study, the results were very close to the experimental measurements from other turbulence models. The results could be used to solve the flow separation problem under different pressure gradients. Figure 5 illustrates the domain in which 3D computation was used in this work. Furthermore, the computational domain was based on the wind tunnel testing dimensions. Two domains were established for the simulation, a rotating domain for the rotor and a stationary domain for wind flow (test section). The boundary settings of the stationary domain were the velocity inlet, outlet pressure, and no-slip wall. Note that the rotary domain had a dimension of 1.1 D, and the diameter size of the rotor was specified as 150 mm. Specifically, the rotor and stationary domains were two distinct parts of the overall computation domain and the frozen rotor model was used to put them in contact. The simulations were run at wind speeds of 6 and 9 m/s, which caused the rotor domain to spin. In addition, an unsteady influence analysis with 40 time steps per revolution rotor was used for all the situations under investigation. The time setup required five hours for four periods, with 40 times steps in each period and six processor cores. The work also implemented the interface model for 3D viscous flutter investigations using the transient rotor stator (TRS 360), which assumes a general connection interface between the revolving and stationary zones. To obtain a decent root mean square (RMS) at each time step, 1 one to three loops of internal iteration with four rotor spins were typically needed.

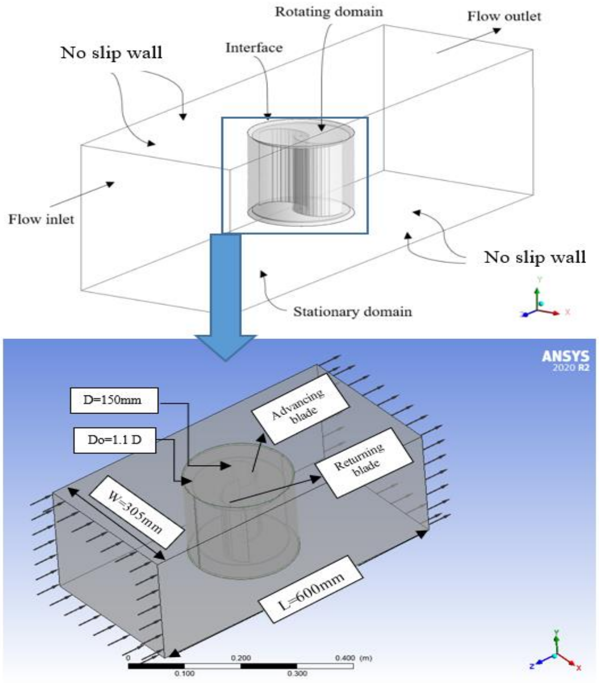

Figure 5. 3D computational domain with boundary conditions.

In this work, we present an unstructured mesh topology and describe how it can be used to efficiently produce a mesh of good quality for both rotating and fixed domains.

As illustrated in Table 1, we analyzed grid independence to determine the skewness and orthogonal quality of the mesh. The total number of elements in the rotary and stationary domains was about 4.056 million, since fine grid meshes were chosen in the end, as shown in Table 2. Inflation on the rotor wall and fine meshing using the tetrahedral technique are depicted in detail in Figure 6. We started from five maximal inflation layers at a 1.1 rate of growth in the test simulation, as shown in Table 2. Under all operating conditions, the thickness of the first layer normal to the wall had to be approximately 0.000122 m to obtain y+ < 5 along all walls. When moving from the inner to the outer domain, the number of grid nodes was reduced by making the outermost grids coarser.

Table 1. The grid independence statistics for the S-ORM model.

Grid	Stationary Domain		Rotating Domain	
	No. of Elements	**No. of Nodes.**	**No. of Elements**	**No. of Nodes.**
Coarse	83,352	27,871	1,757,235	925,883
Medium	194,725	37,101	2,129,990	2,746,720
Fine	231,272	327,557	2,488,752	3,729,226
Extra fine	632,023	235,274	4,391,444	5,254,209

Table 2. Justification of the grid independence statistics.

Density of Mesh	Coarse	Medium	Fine	Extra Fine
Total number of elements	1,840,587	2,324,715	2,720,024	5,023,467
Total number of nodes	953,754	2,783,821	4,056,783	5,489,483
Inflation numbering	5	10	15	20
Growth rate inflation	1.1	1.1	1.1	1.1
Skewness average	0.842	0.839	0.811	0.837
Orthogonal quality average	0.989	0.992	0.994	0.993
Blade sizing (mm)	2.5	2	1.5	1
Rotating circle face sizing (mm)	15	10	5	2.5
Outer domain face sizing (mm)	20	15	10	5

3.3. Experimental Work

The laboratory was equipped with a subsonic open-type wind tunnel, where a drive section with a circular outlet was used for experimental testing, as demonstrated in Figure 7. By adjusting the damper, the wind blowing rate at the wind tunnel's test zone could be varied between 1 and 32 m/s at the user's discretion. As illustrated in Figure 7, an S-ORM was installed in the test section area. Note that the size of this wind tunnel test piece was 600 mm in length, 305 mm in width, and 305 mm in height. Correspondingly, clear polycarbonate boards 10 mm in thickness were bolted to the inside of the wind tunnel to create a contained testing environment. Subsequently, a 500 g range spring balance (analog weighing) was employed to quantify the dynamic torque produced by the Savonius wind rotor shaft. The rope brake dynamometer used a rope coiled around the rim of the rotating pulley to simulate the friction belt, in which the belt rope was attached to the spring balance (counterweight) [62]. However, a digital torque meter placed on the rotor shaft to measure the dynamic torque was not used, which was a limitation of this study. Wind speeds of around 6 and 9 m/s were used in the experiments. When it first started, the turbine model was under no load. The rotating turbine model's speed was slowed by progressively applying a brake load by ratcheting up the tension on the pulley's braking belt. Consequently, forces generated when braking according to the spring weight at different revolutions per minutes (RPMs) were measured and recorded to determine the tip speed ratio (TSR), rotor torque (T), torque coefficient (C_T), and power coefficient (Cp). This procedure was carried out numerous times until the shaft no longer rotated, with each subsequent increment being increased by 1 g. Hence, experiments were conducted repeatedly for each configuration of the turbines to gather datasets. The efficiency of the

S-ORM turbine's power output was compared with the reference model in terms of Cp and C_T. However, qualitative observations using smoke flow visualization at various wind speeds of turbulent flows were not undertaken in the region of the turbine model.

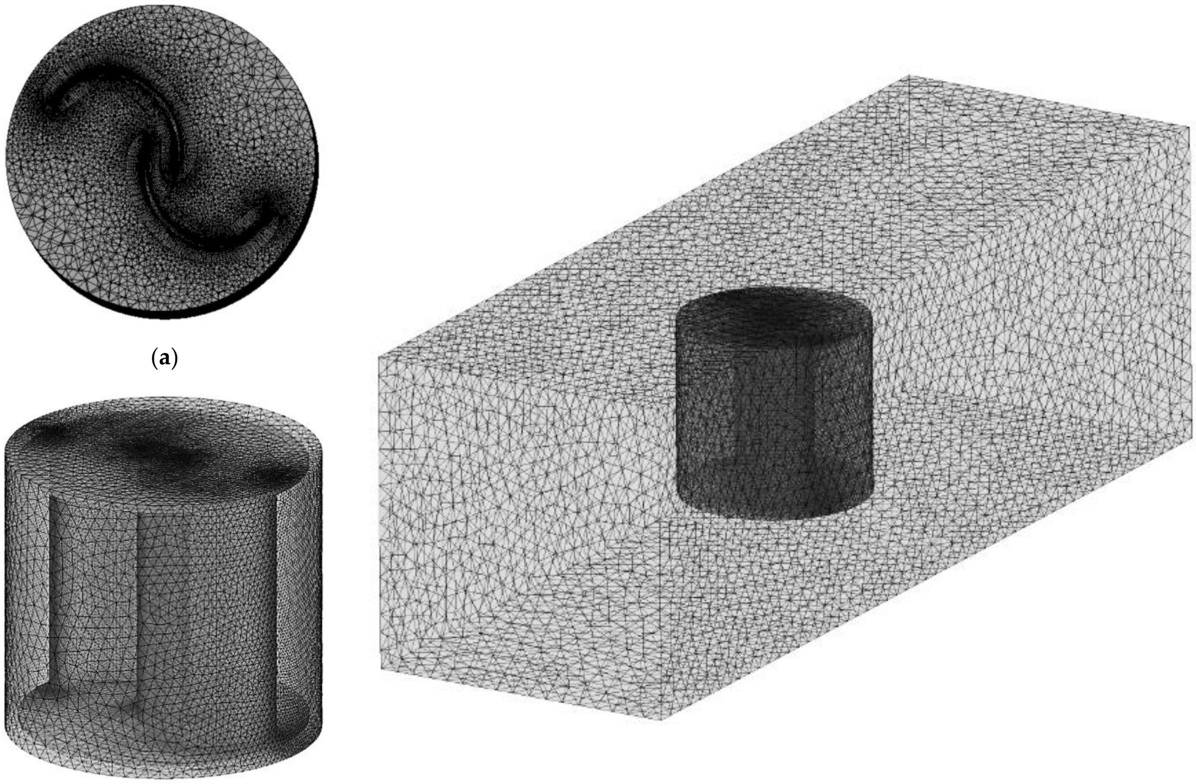

(**a**)

(**b**)

(**c**)

Figure 6. The configuration of the meshes on (**a**) the blades of the turbine, (**b**) the rotating domain, and (**c**) the stationary domain.

Considering the errors throughout the test, the true values for all test outcomes could be determined. The experimental results for this investigation were determined with uncertainties, where conditions of various parameters were considered. Furthermore, the ranges and accuracies of the velocity, turbine speed, and turbine torque were measured and calculated. The measured data provided information about the accuracy of the tachometer (DT-2268), which was ±0.05 for each revolution (RPM). Moreover, the upstream and downstream air velocity of the AF100 open-circuit subsonic wind tunnel was measured using a Pitot static tube. Here, a traversing Pitot tube was adjusted to an accurate measurement. We also calculated uncertainty [63]. Furthermore, we performed a regression analysis for the independent variables of turbine torque and the *TSR* data when carrying out the tests for each regression formula model. Subsequently, their probabilities were assessed, and a confidence interval that covered 95% of the possible outcomes for compliance was generated. Finally, the overall experiment model uncertainty was estimated for each practical replication of the experiment, was and the uncertainties were closely fit and could be accepted.

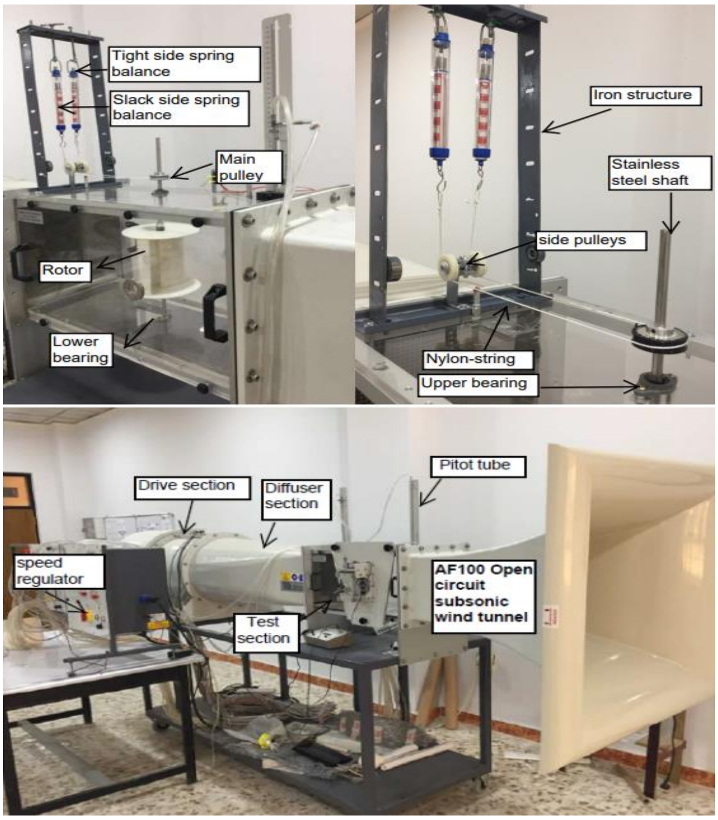

Figure 7. Testing of the Savonius turbine model at the subsonic open-type wind tunnel aerodynamic lab, METPD, Al-Furat Al-Awsat Technical University (ATU).

4. Verification of the Accuracy

Initially, to ensure the accuracy of our model, several different ANSYS CFX software simulation scenarios were developed for the elliptical Savonius turbine, and comparisons were made between the test results and the results given in [48]. Performance was measured relative to the power coefficient (*Cp*) at varying turbine tip speed ratios (*TSR*s). A variety of *TSR*s, ranging from 0.1 to 1.2, were simulated with a wind speed of 9 m/s. The *Cp* reached its maximum value when the *TSR* was 0.7. Previous experimental and numerical results [48] were used to validate the current findings. As shown in Figure 8, ratios ranging from 0.2 to 0.35 and 1.1 to 1.2 were related to the *TSR*, with an error percentage range of less than 5%. These variation percentages may have been due to, first, the different grid resolutions when comparing the present three-dimensional (3D) simulation with a two-dimensional (2D) simulation, which has a higher number of grid cells in 3D simulation computations. Second, different methods of analysis—CFX CFD and fluent—were considered. Finally, they may have been due to the different time steps that were adopted in the current simulation and the previous one. However, no statistically significant change (more than 5%) in the average *Cp* was found in the comparison to the benchmark model. Hence, the maximum overall relative error was less than 9% according to the simulation results obtained from this study; this demonstrates that the numerical method used in this investigation could accurately predict outcomes.

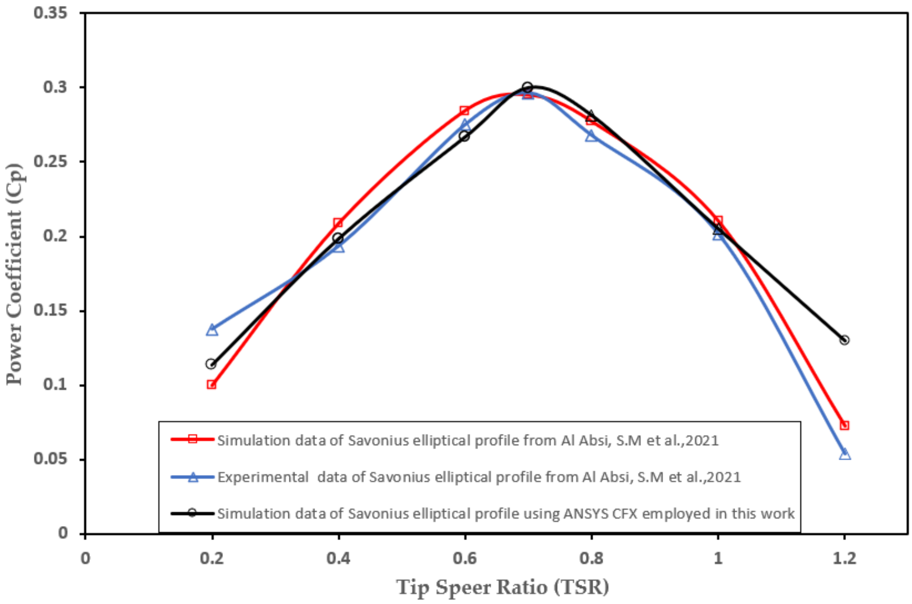

Figure 8. Numerical model verification using *Cp* versus *TSR* [48].

Each time step in the transient simulations was set to twenty iterations, and the optimal solution was convergence, which was achieved as a result of variables approaching [64,65]. Note that all simulations used an absolute convergence criterion to meet the residual targets of 10^{-4} for continuity, velocity components, and turbulent characteristics calculated in CFX. Figure 9 plots the instantaneous torque variation against the accumulated time step for a Savonius turbine at *TSR* = 0.2 to 1.2, corresponding to a maximum *Cp* at *TSR* of 0.7. In fact, the last two subsequent rotations converged after a total of four turbine revolutions. Numerical simulations were used to measure the rotor axis torque coefficient (C_T) for each angular location. The last two complete revolutions were averaged to increase the periodicity stability. This average C_T was employed in the estimate of *Cp* using Equation (3) for all the geometries.

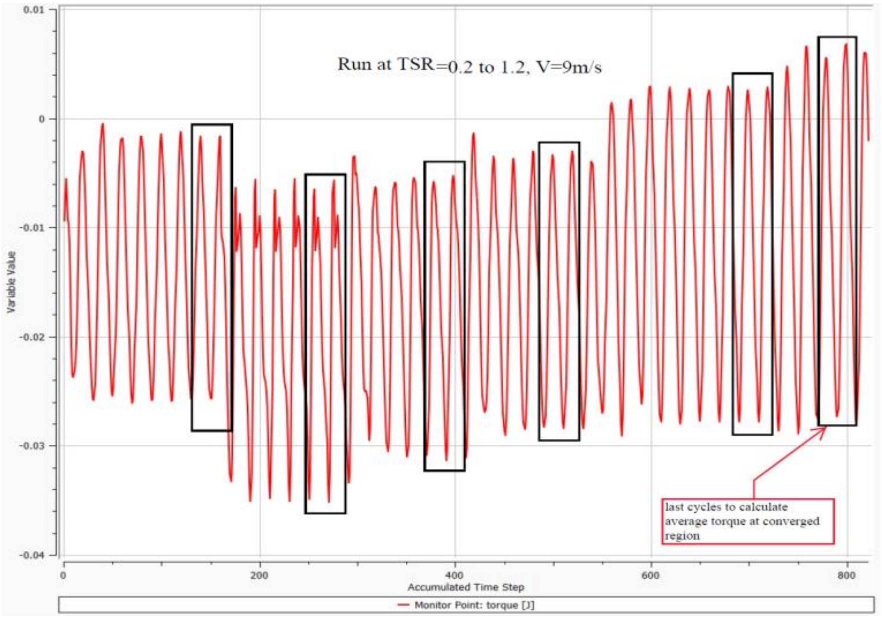

Figure 9. Torque variation against the accumulated time step.

Subsequently, to verify the scale model of the original rotor model (S-ORM) and deduce the link between results, the performance results were compared with the same study's performance results as used previous [48], as shown in Figure 10. Note that the previous results' performance data for wind turbines [48] were scaled to 1:1.3 according to a scale factor (SF) procedure [58]. The matched curves, in which the same behavior was presented, showed a maximum power coefficient (Cp_{max}) variation concerning flow time for a wind speed of 9 m/s at a *TSR* of 0.7, justifying the scaled-down model. Nevertheless, the performance *Cp* curve of the S-ORM was extended to a *TSR* of 1.8, which was greater than the previous research. This means that the present model operated with a wider range of *TSRs* and turbines at peak efficiency.

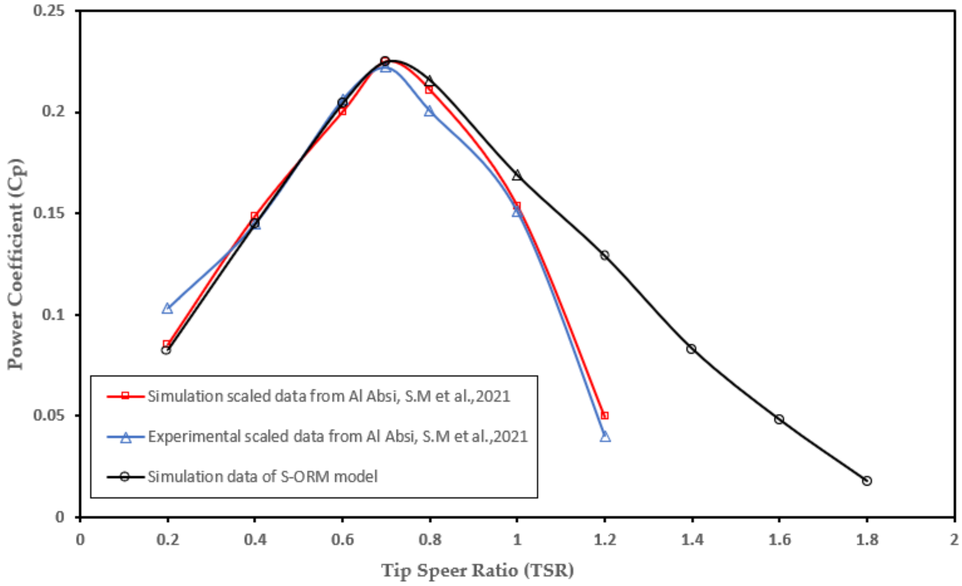

Figure 10. Variations in the scaled Cp_S for the S-ORM, along with the original model [48].

5. Results and Discussion

Principally, this study aimed to produce an overall scaled model of the performance of the original rotor model (S-ORM) turbine using numerical and experimental validation approaches. The second objective was to deduce the optimum modified blade shape configuration and compare it with the S-ORM rotor based on performance.

5.1. S-ORM Validation Study

To validate and approve the computational model of the S-ORM simulation results and validate this study's computational fluid dynamics (CFD) modeling, experimental and simulation tests were utilized for wind velocities of 6 and 9 m/s. This was to determine whether the numerical results were accurate and to determine the best wind velocity. Figures 11 and 12 show the differences in the power coefficient (*Cp*) and torque coefficient (C_T) for some of the interval tip speed ratios (*TSR*s) used, which ranged from 0.2 to 1.8 at an overlap ratio of 0.2. The numerical results for the wind velocity of 6 m/s matched very well with the numerical results for the wind velocity of 9 m/s. The deviation in *Cp* and C_T compared to the experimental data was attributed to fluctuating experimental conditions, and the torque values may have been a result of experimental uncertainty. The maximum power coefficient (Cp_{max}) for the S-ORM numerical results was 0.22 at *TSR* = 0.7, while Cp_{max} for the S-ORM experimental results was 0.21 at *TSR* = 0.7. It was possible to verify that the most effective S-ORM design could be achieved from the CFD study. The maximum relative errors in the values of *Cp* for both the velocities from the simulation results and those from the experimental data for the S-ORM design occurred at *TSRs* ranging from 0.2 to 0.35 and 1.1 to 1.2, with the experimental data being about 8% lower than the simulation results. Hence, this was an acceptable range. Figure 12 illustrates the link between the C_T

and the *TSR*. The graph was inversely related to the *TSR*, as can be observed. Therefore, C_T tended to decrease as *TSR* increased. The average C_T increased linearly with an increase in the *TSR* of approximately 0.7, and the highest average C_T values were reached in all instances with a *TRS* of 0.2. Nonetheless, comparing to the most outstanding *Cp* values for velocities between 6 m/s and 9 m/s, the model with a velocity of 9 m/s performed slightly better than the model with a velocity of 6 m/s. Thus, the newly proposed models used a velocity of 9 m/s.

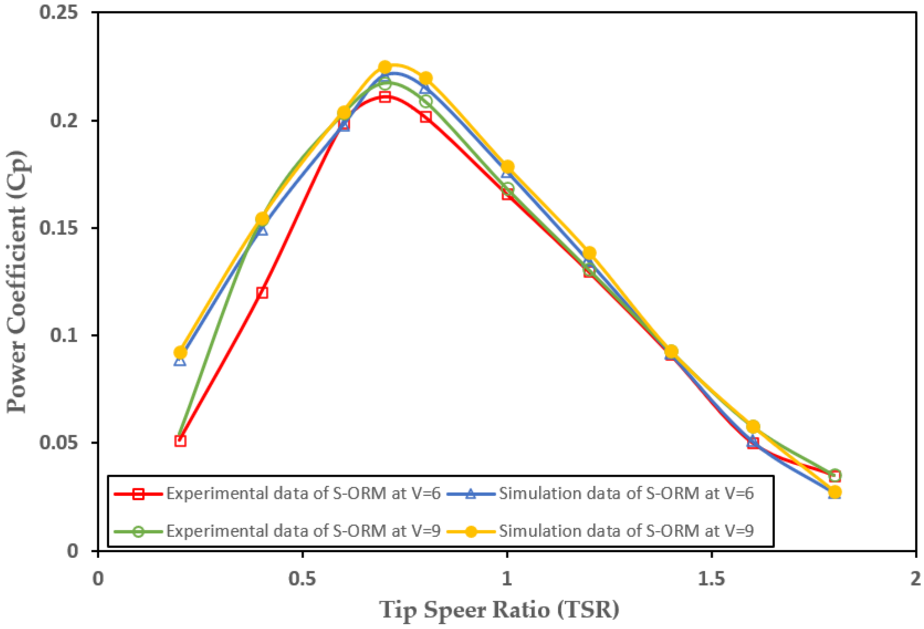

Figure 11. The variations in *Cp* with *TSRs* from 0.2 to 1.8.

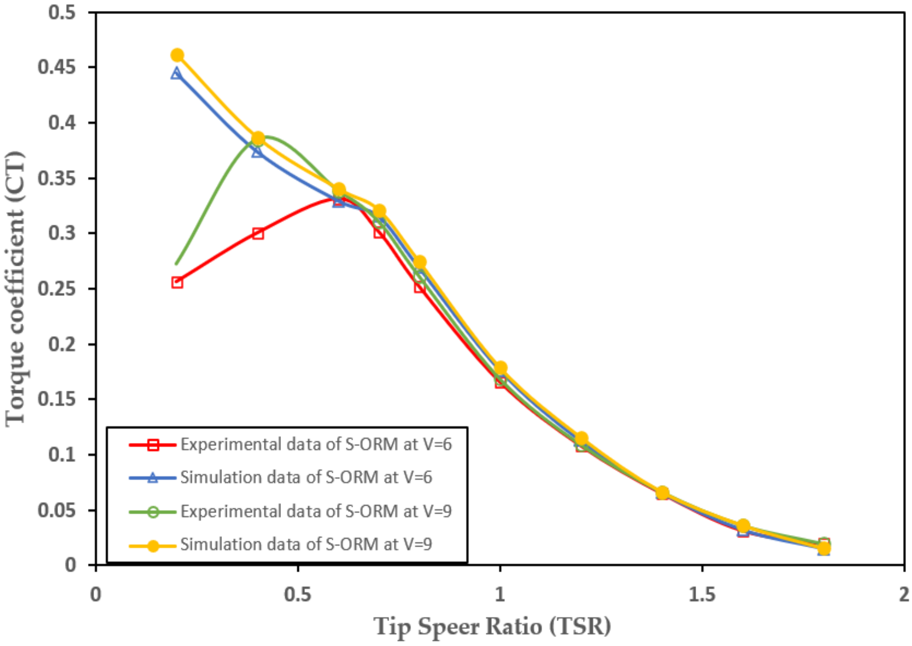

Figure 12. The variations in C_T with *TSRs* from 0.2 to 1.8.

5.2. Effect of Variations in Blade Configrations on the Turbine Performance

The performance of each profile was evaluated in terms of the Cp_{max} achieved for the established *TSR* value equal to 1. Figure 13 shows the results of the tests for each profile.

The Cp values obtained for various configurations showed that the wavy area at the tip and end (WTE), wavy area on the convex blade (WCB), and flow-guiding channel (FGC) models considerably overpredicted the Cp values compared to the others. Furthermore, changes in the wavy area (WA) placements resulted in significant turbulence flow. The addition of the FGC was a characteristic affecting the developing flow close to the entrance. This had an effect on the measured values. Section 5.3 discusses the Cp_{max} obtained for the best three blade profiles with the FGC at $\Phi = 30^{\circ}$, WTE, and WCB models.

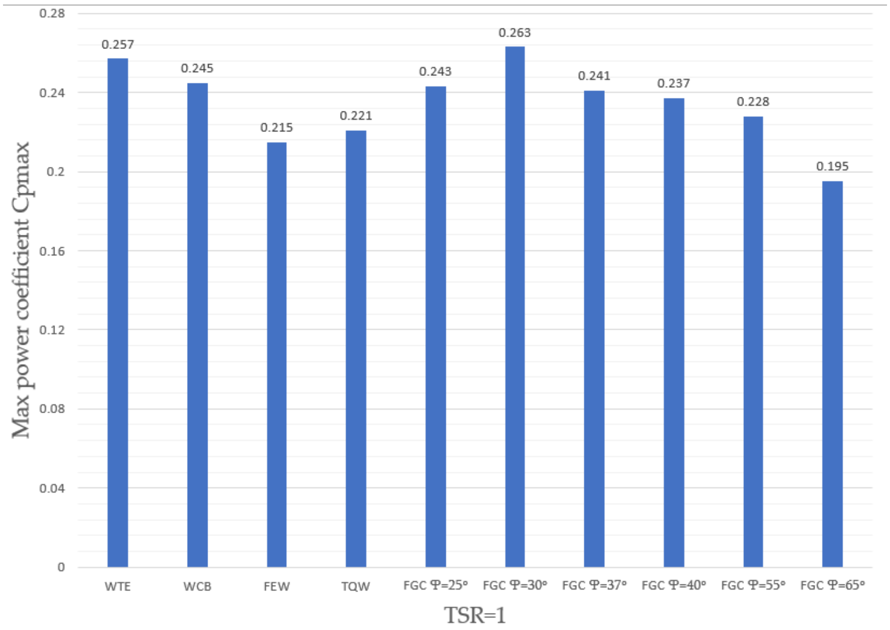

Figure 13. Cp_{max} values obtained from analysis of different blade profiles.

5.3. Velocity Contours for S-ORM, FGC at $\Phi = 30^{\circ}$, WTE, and WCB Models

Figure 14 shows the velocity contour, and variations in the flow velocity of turbine blades in the downstream section are shown in Figure 14. The rotor was permitted to rotate for up to four revolutions, and the plots are from once the rotor had completed its fourth rotation. The velocity of the contour plots' inlet flows matched the boundary condition initialization. High-speed rotating vortices formed at the tip of the advancing blade, and wake zones were included downstream of the rotor. The wake zone started when there was a sudden change in pressure between the regions upstream and downstream of the rotor as a result of the rotor's blockage. As can be seen in Figure 14, the velocity of the benchmark model varied from 5 to 14.5 m/s for the advancing blade and 4 to 9 m/s for the returning blade. The velocity of the FGC at $\Phi = 30^{\circ}$ model ranged from 5 to 15.25 m/s for the advancing blade and from 2.5 to 7 m/s for the returning blade. The velocity of the WTE model varied from 5 to 14.25 m/s for the advancing blade and 3 to 8.25 m/s for the returning blade. The velocity of the WCB model varied from 5 to 14.25 m/s for the advancing blade and 1 to 7 m/s for the returning blade. Figure 14 shows that the new profile models had smoother velocity variations than the benchmark model. The new profile models had lower negative and higher positive moments. Thus, the C_T and Cp of the new models were increased.

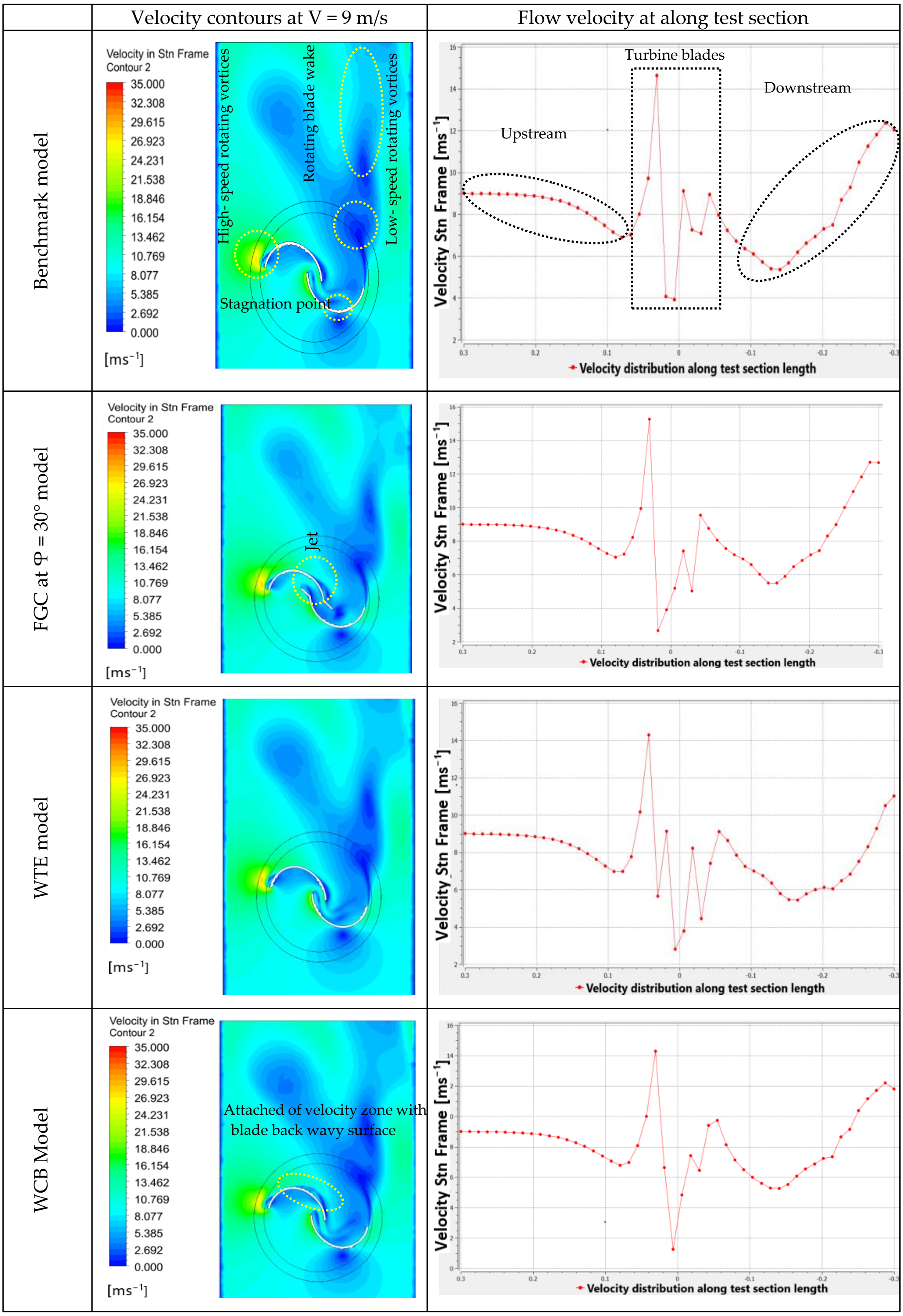

Figure 14. Velocity contours and diagrams for velocity distribution along the test section for *TSR* 1.

5.4. Pressure Contours for S-ORM, FGC at Ƥ = 30°, WTE, and WCB Models

Figure 15 shows the pressure contours at 9 m/s wind speeds for the benchmark S-ORM model and the best three profile models. Due to flow separation, the pressure downstream of the advancing and returning blades was lower. For the upstream pressure, the drag on the returning blade was observed to be greater. The drag force act on both of the turbine's blades; however, the drag acting on the blade that moves forward drives the turbine, while the drag acting on the blade that is moving backward restricts it. The distribution pressure varied along the models' test sections: for the benchmark model, from 80 to -160 N/m^2 for the advancing blade and -160 to 20 N/m^2 for the returning blade. The pressure magnitude of the FGC at Ψ = 300 model varied from 80 to -60 N/m^2 for the advancing blade and -60 to 0 N/m^2 for the returning blade. The pressure magnitude of the WTE model varied from 70 to -150 N/m^2 for the advancing blade and -150 to 10 N/m^2 for the returning blade. The pressure magnitude of the WCB model varied from 70 to -140 N/m^2 for the advancing blade and -140 to -10 N/m^2 for the returning blade. The new models had a lower pressure difference for the advancing blade than the benchmark model, and this increased the new blade profiles' Cp and C_T relative to the benchmark profile. The pressure contour was lower for the concave parts and higher for the convex parts of almost all profiles; this created negative torque for the returning blade, reducing overall performance. However, this differential in pressure between the concave and convex portions of the new-profile blades was less than that in the benchmark profile. Consequently, the new-profile blades performed better than the benchmark profile.

	Pressure contours at V = 9 m/s	Pressure distribution at along test section
Benchmark model	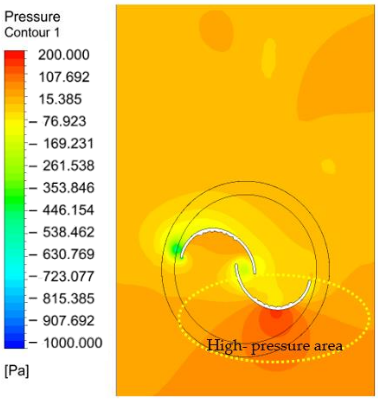	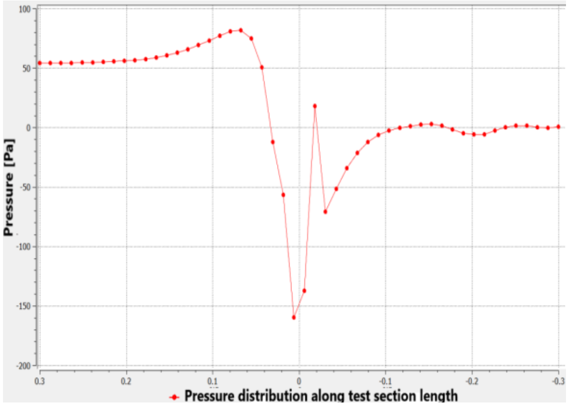
FGC at Ψ = 30° model	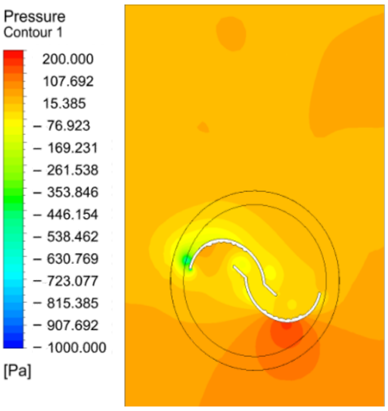	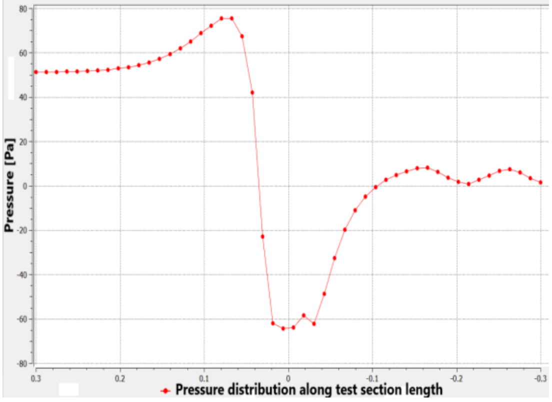

Figure 15. *Cont.*

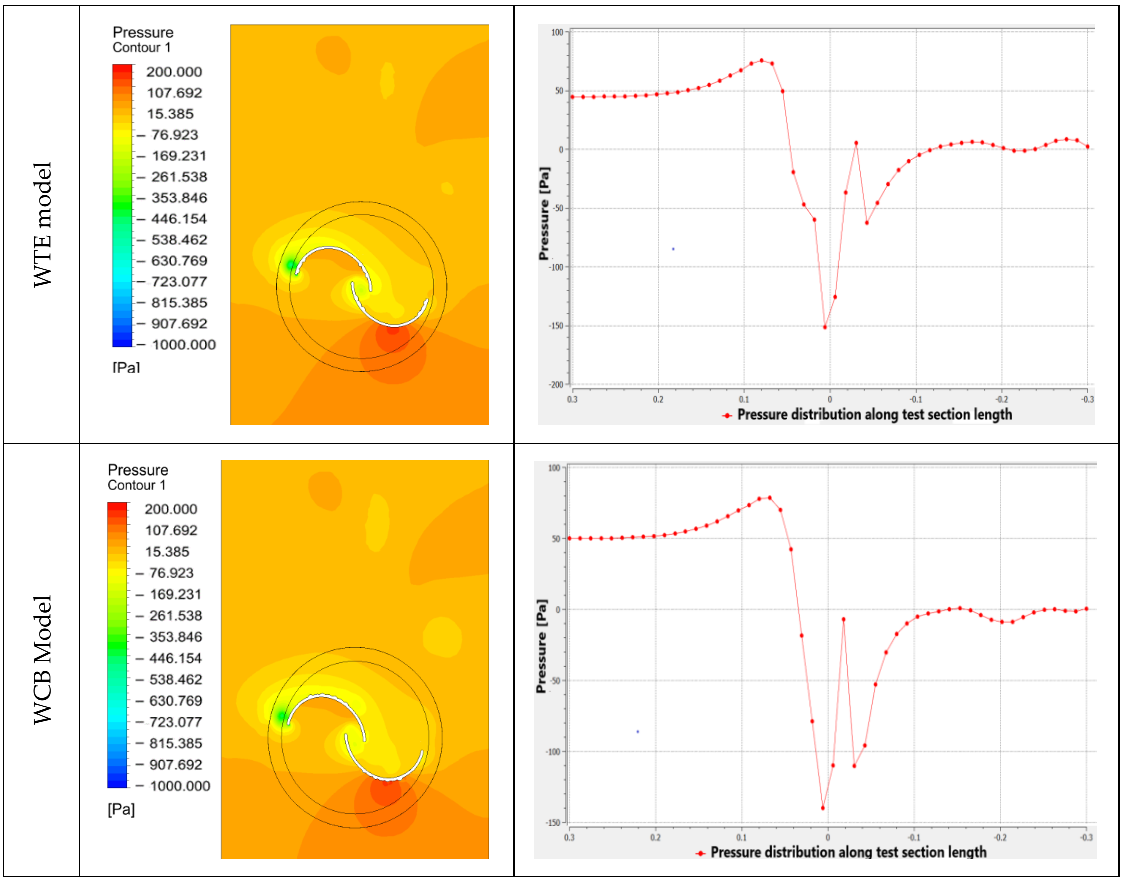

Figure 15. Pressure contours and diagrams for pressure distribution along test section at *TSR* 1.

5.5. *Performance Evaluation of FGC at $\Psi = 30^\circ$, WTE, and WCB Models*

Testing the performance of the updated configuration of the Savonius rotor to evaluate the degree to which it had been improved was the second aim of this study. To validate the suggested turbine design models, the FGC at $\Psi = 30^\circ$, WTE, and WCB models, it was essential to compare the proposed models' performance to that of a well-established turbine design that served as a benchmark design (S-ORM). Accordingly, the three new models (FGC at $\Psi = 30^\circ$, WTE, and WCB) were used for the simulation test, which was undertaken at selected free-stream wind speeds of 9 m/s. Figures 16 and 17 demonstrate the results for the Cp_{max} and C_{Tmax} values for each curve. Comparing the results for the Cp_{max} at $TSR = 0.6$, the FGC at $\Psi = 30^\circ$, WTE, and WCB models performed well with Cp values of 0.22, 0.21, and 0.19, respectively. Furthermore, performance was boosted until it reached its peak at a *TSR* of 1 and Cp_{max} values of 0.263, 0.257, and 0.245, respectively. Subsequently, the *Cp* decreased with increasing turbine speed until it reached its minimal value at a *TSR* of 1.8. Consequently, the highest *Cp* for the FGC at $\Psi = 30^\circ$ model had the best performance with 0.263 for the *Cp* at a *TSR* of 1, which was a 19.5% improvement over the original model. This comprehensive evaluation of the new and modified wind turbines showed that the former achieved higher performance than the standard S-ORM turbine.

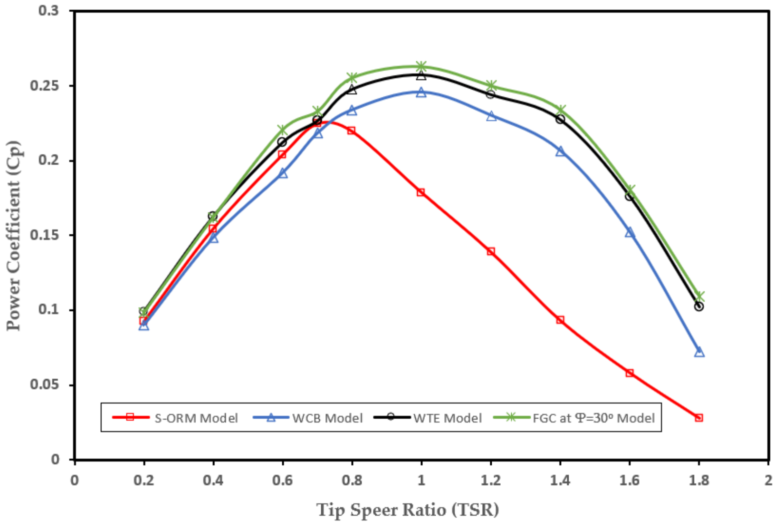

Figure 16. Results of the simulation of the variations in the power coefficients of modified models, along with the S-ORM.

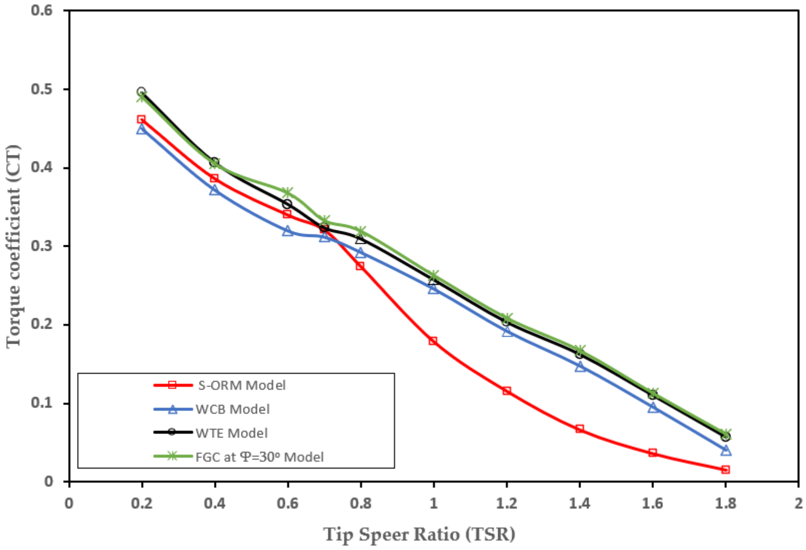

Figure 17. Results of the simulation of the variations in the torque coefficients of modified models, along with the S-ORM.

6. Conclusions

This study investigated the performance of a scaled rotor model of an original model (S-ORM) using three-dimensional (3D) ANSYS CFX and experimental work. Furthermore, it examined the possibility of increasing the output power by changing wavy area positions and adding a flow-guiding channel (FGC) model. Note that the initial step in validating the original 3D simulation method was to use numerical and experimental data from the published literature. A comparison showed that the calculated results agreed well with the experimental ones. The main conclusions can be listed as follows:

1. For comparative investigations, the performance of the benchmark S-ORM model of the basic Savonius wind turbine was calculated numerically;
2. The numerical analysis results and the respective values from the S-ORM model utilized in this work were validated using experimental data. In order to evaluate the accuracy of the S-ORM numerical approach for the mesh and turbulent model employed in this study, the simulation results were compared with experimental data results for the S-ORM model, and the comparison was accepted;

3. The value of *Cps* was found to increase with further increases in the tip speed ratios (TSRs) to 1.8 for all S-ORM configurations;
4. Through analysis of the power coefficient variations, the best design configurations for the profiled blades were identified;
5. It was thus calculated that the values of the power coefficient for the best three out of ten configurations, which were the named the flow-guiding channel (FGC) at $\Psi = 30^\circ$, wavy area at tip and end (WTE), and wavy area on convex blade (WCB) models, were increased by approximately 19.5%, 16.8%, and 12.2%, respectively;
6. The maximum power coefficient obtained with the FGC at $\Psi = 30^\circ$ model was 0.26 at a *TSR* of 1, and the maximum power coefficients of the WTE and WCB models were 0.25 and 0.24, respectively, at the same *TSR*.

In future work, to achieve a higher level of precision with the S-ORM model, researchers need to capture the interaction parameters, collect a more significant amount of data from representative samples by fitting statistical tests for the optimized Savonius wind turbine, and practically validate the turbine's performance. In addition, an experimental investigation is needed to verify the optimal behavior of the improved blade shape. However, according to the findings of this investigation, it appears that the proposed modifications for the elliptical Savonius wind turbine show potential for usage in practical small-scale power generation.

Author Contributions: Conceptualization, K.A.H.A.-G. and F.B.I.A.; methodology, K.A.H.A.-G. and B.A.J.A.-q.; software, A.H.S.A.-S.; validation, F.B.I.A., B.A.J.A.-q. and E.S.T.; data curation, K.A.H.A.-G. and A.H.S.A.-S.; writing—original draft preparation, K.A.H.A.-G.; writing—review and editing, K.A.H.A.-G., F.B.I.A. and B.A.J.A.-q.; supervision, F.B.I.A., B.A.J.A.-q. and E.S.T. All authors have read and agreed to the published version of the manuscript.

Funding: This research received no external funding.

Data Availability Statement: The data presented in this study are available on request from the corresponding author.

Conflicts of Interest: The authors declare no conflict of interest.

Nomenclature

HAWR	Horizontal axis wind rotor	S-ORM	Scaled original rotor model
VAWR	Vertical axis wind rotor	FGC	Flow-guiding channel
WTE	Wavy area at tip and end	WCB	Wavy area on convex blade
TSR	Tip speed ratio	SF	Scale factor
GA	Genetic algorithm	BC	Boundary condition
DIP	Digital image processing	CFD	Computational fluid dynamics
PSO	Particle swarm optimization	RPMs	Revolutions per minute
CD	Drag force	BR	Blockage ratio
CL	Lift force	WA	Wavy area
TW	Theoretical torque	PWA	Position of wavy area
T	Actual torque	FEW	Full-extent wavy area
C_T	Torque coefficient	TQW	Three quarters wavy area
Cp	Power coefficient	FVM	Finite volume method
P	Air density (kg/m^3)	OR	Overlap ratio
A	Wind turbine swept area (m^2)	e	Overlap distance
At	Cross-section area of test section (m^2)	BLN	Blade number
V∞	Incoming wind speed (m/s)	d	Blade radius (m)
V	Wind turbine outer diameter tangent speed (m/s)	H	Blade height (m)
D	Rotor diameter (m)	A/R	Aspect ratios
D0	End plate diameter (m)	y+	Dimensionless wall distance
W	Side tight tension (kg)	S	Side slack (kg)
dr	String nylon diameter (m)	r_p	Pulley radius (m)

References

1. Shah, S.R.; Kumar, R.; Raahemifar, K.; Fung, A.S. Design, modeling and economic performance of a vertical axis wind turbine. *Energy Rep.* **2018**, *4*, 619–623. [CrossRef]
2. Al-Gburi, K.A.H.; Alnaimi, F.B.I.; Al-Quraishi, B.A.; Tan, E.S.; Maseer, M.M. A comparative study review: The performance of Savonius-type rotors. *Mater. Today Proc.* **2021**, *57*, 343–349. [CrossRef]
3. Tummala, A.; Velamati, R.K.; Sinha, D.K.; Indraja, V.; Krishna, V.H. A review on small scale wind turbines. *Renew. Sustain. Energy Rev.* **2016**, *56*, 1351–1371. [CrossRef]
4. Aliferis, A.D.; Jessen, M.S.; Bracchi, T.; Hearst, R.J. Performance and wake of a Savonius vertical-axis wind turbine under different incoming conditions. *Wind Energy* **2019**, *22*, 1260–1273. [CrossRef]
5. Zakaria, A.; Ibrahim, M.S.N. Velocity Pattern Analysis of Multiple Savonius Wind Turbines Arrays. *CFD Lett.* **2020**, *12*, 31–38. [CrossRef]
6. Zakaria, A.; Ibrahim, M.S.N. Enhancement of Wind Farm Power Density by an Oblique Linear Configuration. *J. Adv. Res. Fluid Mech. Therm. Sci.* **2020**, *70*, 77–88. [CrossRef]
7. Zhang, B.; Song, B.; Mao, Z.; Tian, W. A novel wake energy reuse method to optimize the layout for Savonius-type vertical axis wind turbines. *Energy* **2017**, *121*, 341–355. [CrossRef]
8. Zakaria, A. Experimental Evaluation of Multiple Savonius Turbines in Oblique and Cluster Configurations. *Int. J. Emerg. Trends Eng. Res.* **2019**, *7*, 790–793. [CrossRef]
9. Etemadeasl, V.; Esmaelnajad, R.; Farzaneh, B.; Jafari, M. Application of Counter Rotating Rotors for Improving Perfor-mance of Savonius Turbines. *Iran. J. Sci. Technol. -Trans. Mech. Eng.* **2021**, *45*, 473–485. [CrossRef]
10. Etemadeasl, V.; Esmaelnajad, R.; Dizaji, F.F.; Farzaneh, B. A novel configuration for improving the aerodynamic performance of Savonius rotors. *Proc. Inst. Mech. Eng. Part A J. Power Energy* **2018**, *233*, 751–761. [CrossRef]
11. Meziane, M.; Essadiqi, E.; Faqir, M.; Ghanameh, M.F. CFD Study of Unsteady Flow Through Savonius Wind Turbine Clusters. *Int. J. Renew. Energy Res.* **2019**, *9*, 657–666. [CrossRef]
12. Ostos, I.; Ruiz, I.; Gajic, M.; Gómez, W.; Bonilla, A.; Collazos, C. A modified novel blade configuration proposal for a more efficient VAWT using CFD tools. *Energy Convers. Manag.* **2018**, *180*, 733–746. [CrossRef]
13. Sharma, S.; Sharma, R. CFD investigation to quantify the effect of layered multiple miniature blades on the performance of Savonius rotor. *Energy Convers. Manag.* **2017**, *144*, 275–285. [CrossRef]
14. Al-Ghriybah, M.; Zulkafli, M.F.; Didane, D.H.; Mohd, S. The effect of spacing between inner blades on the performance of the Savonius wind turbine. *Sustain. Energy Technol. Assessments* **2021**, *43*, 100988. [CrossRef]
15. Al-Ghriybah, M.; Zulkafli, M.F.; Didane, D.H. Numerical Investigation of Inner Blade Effects on the Conventional Savonius Rotor with External Overlap. *J. Sustain. Dev. Energy Water Environ. Syst.* **2020**, *8*, 561–576. [CrossRef]
16. Kurniawan, Y.; Tjahjana, D.D.D.P.; Santoso, B. Experimental Study of Savonius Wind Turbine Performance with Blade Layer Addition. *J. Adv. Res. Fluid Mech. Therm. Sci.* **2020**, *69*, 23–33. [CrossRef]
17. Antar, E.; Elkhoury, M. Parametric sizing optimization process of a casing for a Savonius Vertical Axis Wind Turbine. *Renew. Energy* **2019**, *136*, 127–138. [CrossRef]
18. Mohammadi, M.; Ramadan, A.; Mohamed, M. Numerical investigation of performance refinement of a drag wind rotor using flow augmentation and momentum exchange optimization. *Energy* **2018**, *158*, 592–606. [CrossRef]
19. He, D.Q.; Bai, H.L.; Chan, C.M.; Li, K.M. Performance-based Optimizations on Savonius-type Vertical-axis Wind Tur-bines using Genetic Algorithm. *Energy Procedia* **2019**, *158*, 643–648. [CrossRef]
20. Mandal, A.K.; Rana, K.B.; Tripathi, B. Experimental study on performance improvement of a Savonius turbine by equipping with a cylindrical cowling. *Energy Sources Part A Recover. Util. Environ. Eff.* **2020**, 1–19. [CrossRef]
21. Manganhar, A.L.; Rajpar, A.H.; Luhur, M.R.; Samo, S.R.; Manganhar, M. Performance analysis of a savonius vertical axis wind turbine integrated with wind accelerating and guiding rotor house. *Renew. Energy* **2019**, *136*, 512–520. [CrossRef]
22. Dwi Prija Tjahjana, D.D.; Hadi, S.; Wicaksono, Y.A.; Mungil Kurniawati, D.; Fahrudin, F.; Satrio Utomo, I.; Cahyono SI Prasetyo, A. Study on performance improvement of the Savonius wind turbine for Urban Power System with Omni-Directional Guide Vane (ODGV). *J. Adv. Res. Fluid Mech. Therm. Sci.* **2019**, *55*, 126–135.
23. Yahya, W.; Ziming, K.; Juan, W.; Al-Nehari, M.; Tengyu, L.; Qichao, R.; Alhayani, B. Study the influence of using guide vanes blades on the performance of cross-flow wind turbine. *Appl. Nanosci.* **2021**, 1–10. [CrossRef]
24. Yuwono, T.; Sakti, G.; Aulia, F.N.; Wijaya, A.C. Improving the performance of Savonius wind turbine by installation of a circular cylinder upstream of returning turbine blade: Improving the Performance of Savonius Wind Turbine. *Alex. Eng. J.* **2020**, *59*, 4923–4932. [CrossRef]
25. Yahya, W.; Ziming, K.; Juan, W.; Qurashi, M.S.; Al-Nehari, M.; Salim, E. Influence of tilt angle and the number of guide vane blades towards the Savonius rotor performance. *Energy Rep.* **2021**, *7*, 3317–3327. [CrossRef]
26. Grönman, A.; Tiainen, J.; Jaatinen-Värri, A. Experimental and analytical analysis of vaned savonius turbine performance under different operating conditions. *Appl. Energy* **2019**, *250*, 864–872. [CrossRef]
27. Grönman, A.; Backman, J.; Hansen-Haug, M.; Laaksonen, M.; Alkki, M.; Aura, P. Experimental and numerical analysis of vaned wind turbine performance and flow phenomena. *Energy* **2018**, *159*, 827–841. [CrossRef]
28. Sheikh, H.M.; Shabbir, Z.; Ahmed, H.; Waseem, M.H.; Sheikh, M.Z. Computational fluid dynamics analysis of a modified Savonius rotor and optimization using response surface methodology. *Wind Eng.* **2017**, *41*, 285–296. [CrossRef]

29. Borzuei, D.; Moosavian, S.F.; Farajollahi, M. On the Performance Enhancement of the Three-Blade Savonius Wind Turbine Implementing Opening Valve. *J. Energy Resour. Technol.* **2021**, *143*, 051301. [CrossRef]
30. Marinić-Kragić, I.; Vučina, D.; Milas, Z. Concept of flexible vertical-axis wind turbine with numerical simulation and shape optimization. *Energy* **2018**, *167*, 841–852. [CrossRef]
31. Zhou, Q.; Xu, Z.; Cheng, S.; Huang, Y.; Xiao, J. Innovative Savonius rotors evolved by genetic algorithm based on 2D-DCT encoding. *Soft Comput.* **2018**, *22*, 8001–8010. [CrossRef]
32. Ramadan, A.; Yousef, K.; Said, M.; Mohamed, M. Shape optimization and experimental validation of a drag vertical axis wind turbine. *Energy* **2018**, *151*, 839–853. [CrossRef]
33. Chan, C.M.; Bai, H.L.; He, D.Q. Blade shape optimization of the Savonius wind turbine using a genetic algo-rithm. *Appl. Energy* **2018**, *213*, 148–157. [CrossRef]
34. Mohammadi, M.; Lakestani, M.; Mohamed, M. Intelligent parameter optimization of Savonius rotor using Artificial Neural Network and Genetic Algorithm. *Energy* **2018**, *143*, 56–68. [CrossRef]
35. Zheng, Y.; Bai, H.; Chan, C. Optimization of Savonius turbine clusters using an evolutionary based Genetic Algorithm. *Energy Procedia* **2019**, *158*, 637–642. [CrossRef]
36. Masdari, M.; Tahani, M.; Naderi, M.H.; Babayan, N. Optimization of airfoil Based Savonius wind turbine using coupled discrete vortex method and salp swarm algorithm. *J. Clean. Prod.* **2019**, *222*, 47–56. [CrossRef]
37. Zhang, B.; Song, B.; Mao, Z.; Tian, W.; Li, B.; Li, B. A Novel Parametric Modeling Method and Optimal Design for Savonius Wind Turbines. *Energies* **2017**, *10*, 301. [CrossRef]
38. Chang, T.-L.; Tsai, S.-F.; Chen, C.-L. Optimal Design of Novel Blade Profile for Savonius Wind Turbines. *Energies* **2021**, *14*, 3484. [CrossRef]
39. Doerffer, K.; Telega, J.; Doerffer, P.; Hercel, P.; Tomporowski, A. Dependence of Power Characteristics on Savonius Rotor Segmentation. *Energies* **2021**, *14*, 2912. [CrossRef]
40. Bhayo, B.A.; Al-Kayiem, H.H. Experimental characterization and comparison of performance parameters of S-rotors for standalone wind power system. *Energy* **2017**, *138*, 752–763. [CrossRef]
41. Tjahjana, D.D.D.P.; Arifin, Z.; Suyitno, S.; Juwana, W.E.; Prabowo, A.R.; Harsito, C. Experimental study of the effect of slotted blades on the Savonius wind turbine performance. *Theor. Appl. Mech. Lett.* **2021**, *11*, 100249. [CrossRef]
42. Chaisiriroj, P.; Tinnachote, N.; Usajantragul, S.; Leephakpreeda, T. Experimental Performance Investigation of Optimal Vertical Axis Wind Turbines under Actual Wind Conditions in Thailand. *Energy Procedia* **2017**, *138*, 651–656. [CrossRef]
43. Zadeh, M.N.; Safari, M.P.S.; Gholinia, S.M.; Taheri, S.M.A. Performance assessment and optimization of a helical Savonius wind turbine by modifying the Bach's section. *SN Appl. Sci.* **2021**, *3*, 739. [CrossRef]
44. Mosbahi, M.; Mosbahi, M.; Chouaibi, Y.; Driss, Z. Performance Improvement in a Helical Savonius Wind Rotor. *Arab. J. Sci. Eng.* **2020**, *45*, 9305–9323. [CrossRef]
45. Damak, A.; Driss, Z.; Abid, M. Optimization of the helical Savonius rotor through wind tunnel experiments. *J. Wind Eng. Ind. Aerodyn.* **2018**, *174*, 80–93. [CrossRef]
46. Alom, N.; Saha, U.K. Drag and Lift Characteristics of a Novel Elliptical-Bladed Savonius Rotor with Vent Augmenters. *J. Sol. Energy Eng.* **2019**, *141*, 051007. [CrossRef]
47. Alom, N.; Saha, U.K. Examining the Aerodynamic Drag and Lift Characteristics of a Newly Developed Elliptical-Bladed Savonius Rotor. *J. Energy Resour. Technol.* **2019**, *141*, 051201. [CrossRef]
48. Al Absi, S.M.; Jabbar, A.H.; Mezan, S.O.; Al-Rawi, B.A.; Al_Attabi, S.T. An experimental test of the performance enhancement of a Savonius turbine by modifying the inner surface of a blade. *Mater. Today Proc.* **2021**, *42*, 2233–2240. [CrossRef]
49. Elmekawy, A.M.N.; Saeed, H.A.H.; Kassab, S.Z. Performance enhancement of Savonius wind turbine by blade shape and twisted angle modifications. *Proc. Inst. Mech. Eng. Part A J. Power Energy* **2021**, *235*, 1487–1500. [CrossRef]
50. El-Askary, W.; Saad, A.S.; AbdelSalam, A.M.; Sakr, I. Experimental and Theoretical Studies for Improving the Performance of a Modified Shape Savonius Wind Turbine. *J. Energy Resour. Technol.* **2020**, *142*, 1211303. [CrossRef]
51. Saad, A.S.; El-Sharkawy, I.I.; Ookawara, S.; Ahmed, M. Performance enhancement of twisted-bladed Savonius vertical axis wind turbines. *Energy Convers. Manag.* **2020**, *209*, 112673. [CrossRef]
52. Tahani, M.; Rabbani, A.; Kasaeian, A.; Mehrpooya, M.; Mirhosseini, M. Design and numerical investigation of Savonius wind turbine with discharge flow directing capability. *Energy* **2017**, *130*, 327–338. [CrossRef]
53. D'Alessandro, V.; Montelpare, S.; Ricci, R.; Secchiaroli, A. Unsteady Aerodynamics of a Savonius wind rotor: A new computational approach for the simulation of energy performance. *Energy* **2010**, *35*, 3349–3363. [CrossRef]
54. Nasef, M.; El-Askary, W.; AbdEL-Hamid, A.; Gad, H. Evaluation of Savonius rotor performance: Static and dynamic studies. *J. Wind Eng. Ind. Aerodyn.* **2013**, *123*, 1–11. [CrossRef]
55. Kulak, M.; Karczewski, M.; Olasek, K.; Jozwik, K. CFD analysis of Diffuser Augmented Wind Turbine model for wind tunnel investigation. In Proceedings of the IECON 2016 42nd Annual Conference of the IEEE Industrial Electronics Society, Florence, Italy, 23–26 October 2016; pp. 5538–5543. [CrossRef]
56. Roy, S.; Saha, U.K. An adapted blockage factor correlation approach in wind tunnel experiments of a Savonius-style wind turbine. *Energy Convers. Manag.* **2014**, *86*, 418–427. [CrossRef]
57. Mauro, S.; Brusca, S.; Lanzafame, R.; Messina, M. CFD modeling of a ducted Savonius wind turbine for the evaluation of the blockage effects on rotor performance. *Renew. Energy* **2019**, *141*, 28–39. [CrossRef]

58. Giahi, M.H.; Dehkordi, A.J. Investigating the influence of dimensional scaling on aerodynamic characteristics of wind turbine using CFD simulation. *Renew. Energy* **2016**, *97*, 162–168. [CrossRef]
59. Akwa, J.V.; Vielmo, H.A.; Petry, A.P. A review on the performance of Savonius wind turbines. *Renew. Sustain. Energy Rev.* **2012**, *16*, 3054–3064. [CrossRef]
60. Sharma, S.; Sharma, R.K. Performance improvement of Savonius rotor using multiple quarter blades—A CFD investigation. *Energy Convers. Manag.* **2016**, *127*, 43–54. [CrossRef]
61. Zhao, D.; Han, N. Optimizing overall energy harvesting performances of miniature Savonius-like wind harvesters. *Energy Convers. Manag.* **2018**, *178*, 311–321. [CrossRef]
62. Talukdar, P.K.; Sardar, A.; Kulkarni, V.; Saha, U.K. Parametric analysis of model Savonius hydrokinetic turbines through experimental and computational investigations. *Energy Convers. Manag.* **2018**, *158*, 36–49. [CrossRef]
63. Moffat, R.J. Describing the uncertainties in experimental results. *Exp. Therm. Fluid Sci.* **1988**, *1*, 3–17. [CrossRef]
64. Lee, J.-H.; Lee, Y.-T.; Lim, H.-C. Effect of twist angle on the performance of Savonius wind turbine. *Renew. Energy* **2016**, *89*, 231–244. [CrossRef]
65. Chemengich, S.J.; Kassab, S.Z.; Lotfy, E.R. Effect of the variations of the gap flow guides geometry on the savonius wind turbine performance: 2D and 3D studies. *J. Wind Eng. Ind. Aerodyn.* **2021**, *222*, 104920. [CrossRef]